Origin of zigzag antiferromagnetic order in XPS_3 (X = Fe, Ni) monolayers

Ping Li,[1,2,*] Xueyang Li,[3,4,*] Junsheng Feng,[5] Jinyang Ni,[3,4] Zhi-Xin Guo,[1,†] and Hongjun Xiang[3,4,6,‡]

[1]*State Key Laboratory for Mechanical Behavior of Materials, School of Materials Science and Engineering, Xi'an Jiaotong University, Xi'an, Shaanxi 710049, China*

[2]*State Key Laboratory for Surface Physics and Department of Physics, Fudan University, Shanghai 200433, China*

[3]*Key Laboratory of Computational Physical Sciences (Ministry of Education), Institute of Computational Physical Sciences, and Department of Physics, Fudan University, Shanghai 200433, China*

[4]*Shanghai Qi Zhi Institution, Shanghai 200030, China*

[5]*School of Physics and Materials Engineering, Hefei Normal University, Hefei 230601, China*

[6]*Collaborative Innovation Center of Advanced Microstructures, Nanjing 210093, China*

(Received 29 January 2024; accepted 3 June 2024; published 13 June 2024)

Recently, two monolayer magnetic materials, i.e., $FePS_3$ and $NiPS_3$, have been successfully fabricated. Despite them having the same atomic structure, the two monolayers exhibit distinct magnetic properties. $FePS_3$ holds an out-of-plane zigzag antiferromagnetic (AFM-ZZ) structure, while $NiPS_3$ exhibits an in-plane AFM-ZZ structure. However, there is no theoretical model that can properly describe its magnetic ground state due to the lack of a full understanding of its magnetic interactions. Here, by combining the first-principles calculations and the newly developed machine learning method, we construct an exact spin Hamiltonian of the two magnetic materials. Different from the previous studies that failed to fully consider the spin-orbit-coupling effect, we find that the AFM-ZZ ground state in $FePS_3$ is stabilized by competing ferromagnetic nearest-neighbor and antiferromagnetic third-nearest-neighbor exchange interactions and combining single-ion anisotropy. In contrast, the often ignored nearest-neighbor biquadratic exchange is responsible for the in-plane AFM-ZZ ground state in $NiPS_3$. We additionally calculate the spin-wave spectrum of the AFM-ZZ structure in the two monolayers based on the exact spin Hamiltonian, which can be directly verified by the experimental investigation. Our work provides a theoretical framework for the origin of the AFM-ZZ ground state in two-dimensional materials.

DOI: 10.1103/PhysRevB.109.214418

I. INTRODUCTION

Since the discovery of graphene, two-dimensional (2D) atomic crystals have seen a surge of interest due to their highly tunable physical properties and great potential in scalable device applications [1–9]. The recent reports of ferromagnetic (FM) order in two different 2D crystals $Cr_2Ge_2Te_6$ [10] and CrI_3 [11] mark the beginning of a new chapter in the remarkable field of 2D materials. These discoveries significantly extend the list of electronically ordered 2D crystals, which includes superconductors [12,13], charge density wave materials [14], topological insulators [15], and ferroelectrics [16–18]. The physical mechanisms of 2D FM materials has been described by the bilinear spin Hamiltonians (including Heisenberg symmetric exchange, Dzyaloshinskii-Moriya antisymmetric exchange, anisotropic symmetric exchange, and single-ion anisotropy) [19].

Among 2D materials, transition-metal trichalcogenides XPS_3 (here we focus on X = Fe, Ni) are particularly interesting. They all have the same monoclinic structure with a space group $C2/m$, where layers on the ab plane are coupled by a weak van der Waals force along the c axis [20]. In these materials, the metal atoms are enclosed in octahedra formed by the sulfur atoms and there is a phosphorus doublet at the center of the honeycomb hexagons. Due to the slightly distorted octahedral crystal field, the $3d^6$ electrons of Fe hold the filled e_g, a_{1g}, and e'_g majority states and half-filled e'_g minority states, and the $3d^8$ electrons of Ni hold the filled a_{1g} and e'_g majority and minority states and filled e_g minority states. This feature makes $FePS_3$ and $NiPS_3$ semiconducting materials with the magnetic moment of $4\mu_B$ per Fe and $2\mu_B$ per Ni, respectively. Neutron scattering and Raman experiments reported that $FePS_3$ exhibits an Ising-type zigzag antiferromagnetic (AFM-ZZ) order down to the monolayer limit [21–24], whereas in-plane AFM-ZZ order was observed in $NiPS_3$ [25–27]. Theoretically, the origin of AFM-ZZ order in XPS_3 is still under debate. For example, Kim and Park reported that the dipolar anisotropy is essential to stabilize the AFM-ZZ state for YPS_3 (Y= Mn, Fe, Ni) [28], while Amirabbasi and Kratzer proposed that the orbital ordering induced by a variation of Fe-Fe pair distance is responsible for the AFM-ZZ order in $FePS_3$ [29]. Therefore, a more systematic study of the spin Hamiltonian of 2D XPS_3 materials, which can exactly reveal the origin of their AFM-ZZ magnetic ground state, is highly desirable.

In this work we explore the origin of the AFM-ZZ ground state in 2D XPS_3 by constructing an exact spin Hamiltonian, which is realized by combining the first-principles

*These authors contributed equally to this work.
†Contact author: zxguo08@xjtu.edu.cn
‡Contact author: hxiang@fudan.edu.cn

calculations [density functional theory (DFT)] [30] and the newly developed machine learning method. We find that the AFM-ZZ ground state in $FePS_3$ and $NiPS_3$ originates from different mechanisms. The AFM-ZZ order in $FePS_3$ is established by the competition of FM nearest-neighbor (NN) and AFM third-NN exchange interactions between the Ising-like Fe spins, whereas the usually overlooked biquadratic exchange is the dominating factor for the AFM-ZZ order in $NiPS_3$. Moreover, the degenerate d_{xy} and $d_{x^2-y^2}$ orbitals of Fe lead to a positive magnetocrystalline anisotropy energy (MAE) value and thus an out-of-plane magnetism in $FePS_3$, whereas in $NiPS_3$ the majority of d orbitals of Ni contribute to a negative MAE, leading to an in-plane magnetic ground state. Finally, we predict the spin-wave spectra of $FePS_3$ and $NiPS_3$, which are expected to be observed in the experiments. Moreover, understanding the magnetic ground state and constructing its spin Hamiltonian are the basis of investigating magnetic properties of a material, such as anomalous Hall effect, magnetic transition temperature, thermodynamic property, spin dynamical property, and excited states. The proposed spin Hamiltonian for a 2D AFM-ZZ ground magnetic state provides a theoretical framework for the study of the magnetic properties of other 2D materials with the AFM-ZZ ground state.

II. COMPUTATIONAL METHODS

Our first-principles calculations are performed based on the projected augmented-wave method [31] encoded in the Vienna *ab initio* simulation package [32]. Because the Perdew-Burke-Ernzerhof (PBE) exchange-correlation functional is unable to give rise to the correct d-orbital occupied state of $FePS_3$, the local density approximation (LDA) exchange-correlation functional is used for the $FePS_3$ calculations [33]. Nonetheless, the PBE exchange-correlation functional is adopted for the $NiPS_3$ calculations [34]. The plane-wave basis with a kinetic energy cutoff of 500 eV is employed. To describe strongly correlated $3d$ electrons of Fe and Ni, the LDA $+ U$ and generalized gradient approximation (GGA $+ U$) methods are applied with the effective U value ($U_{\text{eff}} = U - J$) of 4 eV [21,28,35], respectively. The spin-orbit coupling (SOC) effect is considered in the training set and testing set calculations of $FePS_3$, whereas it is not taken into account in the training set and testing set calculations of $NiPS_3$. This is because the doubly degenerate e'_g minority states are only filled with one electron for $FePS_3$, which is easily perturbed by orbital contributions. However, due to the filled a_{1g} and e'_g states and half-filled e_g states of Ni $3d^8$ electrons in $NiPS_3$, the SOC effect can be neglected. A vacuum of 20 Å is set along the c axis to avoid the interaction between the sheet and its periodic images. The convergence criteria of the total energy and the force are set to be 10^{-6} eV and -0.01 eV/Å, respectively.

Spin-exchange parameters are obtained by combing the machine learning method for constructing Hamiltonians (MLMCH) [30,36], the four-state method [19,37], and the modified four-state mapping method [37]. By applying machine learning approaches and statistical analysis, the MLMCH is able to efficiently and correctly find the most important interaction terms among thousands of candidate terms. We randomly generate 200 magnetic configurations and analyze the nonequivalent magnetic interaction. The training set and the testing set contain 150 and 50 sets of data, respectively. In picking important magnetic exchange interactions, the truncation distances of second- and fourth-order terms are both set to 20 bohrs. For $FePS_3$, we consider the SOC interaction, but not for $NiPS_3$. After symmetry analysis, the number of possible nonequivalent parameters $p_{\max}$ is 24 for $FePS_3$ and 76 for $NiPS_3$ (including a constant term). For the four-state method and the MLMCH, we use a $3 \times 3 \times 1$ supercell of monolayer XPS_3 to extract the related magnetic parameters. In our parallel tempering Monte Carlo (PTMC) simulations of the spin Hamiltonian [38,39] with the PASP package [40], a $36 \times 36 \times 1$ supercell of the unit cell is adopted for monolayer XPS_3. Similar results are obtained with larger supercells ($48 \times 48 \times 1$) to estimate the magnetic critical temperature. The number of replicas is set to 80. The spin-wave spectrum is calculated within the linear spin wave theory (LSWT) using the SPINW software package [41].

III. RESULTS AND DISCUSSION

A. Spin Hamiltonian

We first calculate the relative energies for four possible magnetic configurations in a $2 \times 2 \times 1$ supercell (see Fig. 1), namely, the FM, Néel antiferromagnetic (AFM-N), AFM-ZZ, and stripy antiferromagnetic (AFM-ST) structures, using two different procedures [42]. One is the structure optimized with the FM spin order (see Fig. 1) and the other uses the structure optimized with the FM, AFM-N, AFM-ZZ, and AFM-ST spin order, respectively (see Fig. S1 in the Supplemental Material [43]). As shown in Fig. 1 herein and Fig. S1 in [43], the two procedures give similar energetics with the AFM-ZZ order being most stable, which agrees well with previous studies [28,29]. This result also indicates that spin-lattice coupling can be neglected. Hereafter, we consider only the spin degrees of freedom.

We then construct the exact spin Hamiltonian based on the calculations of the MLMCH. After extensive calculations, we obtain several most significant interaction terms among thousands of candidates for the spin Hamiltonian. It is found that the spin Hamiltonian of XPS_3 monolayers has a general form

$$H = \sum_{\langle i,j \rangle} [J_1 S_i \cdot S_j + K(S_i \cdot S_j)^2] + \sum_{\langle i,l \rangle} J_2 S_i \cdot S_l + \sum_{\langle i,k \rangle} J_3 S_i \cdot S_k - \sum_i A_z S_{iz}^2, \quad (1)$$

where J_1, K, J_2, J_3, and A_z are the first-NN Heisenberg exchange parameter, first-NN biquadratic exchange parameter, second-NN Heisenberg exchange parameter, third-NN Heisenberg exchange parameter, and single-ion anisotropy parameter, respectively. The negative and positive values represent FM and AFM interactions for the Heisenberg interaction, respectively. As shown in Table I, in the XPS_3 monolayers the NN FM exchange interactions J_1 and third-NN AFM interactions J_3 are very strong, whereas the second-NN interactions J_2 can be neglected. Note that the unusually large J_3 in $FePS_3$ can be obtained via DFT calculations provided the SOC effect is additionally considered

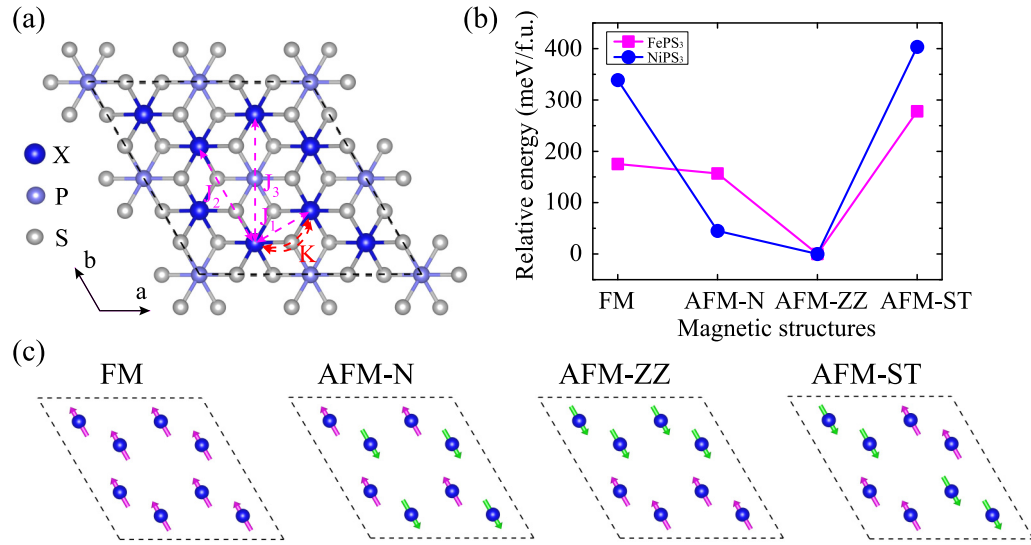

FIG. 1. (a) Crystal structure of monolayer $X\mathrm{PS_3}$, along with magnetic exchange paths, i.e., first-neighbor (J_1), first-neighbor biquadratic (K), second-neighbor (J_2), and third-neighbor (J_3) exchange interactions. (b) Calculated relative energies for various magnetic structures of monolayer $\mathrm{FePS_3}$ by the LDA + U + SOC ($\mathrm{NiPS_3}$ by GGA + U) method using the structure optimized with the FM order. Here the AFM-ZZ state is chosen as the energy reference. (c) Schematic top view of various magnetic structures only containing magnetic atoms.

in the atomic-structure optimization procedure, which was ignored in previous studies [28,29,35]. It is also noticed that both $\mathrm{FePS_3}$ and $\mathrm{NiPS_3}$ have significant biquadratic interactions.

On the other hand, in order to confirm the above results of the MLMCH, we further calculate the interaction parameters by means of the four-state method [19,33] using a $3 \times 3 \times 1$ supercell. As shown in Table I, the spin Hamiltonian parameters obtained by the two methods are consistent. In addition, we also use TB2J software [44] based on the magnetic force method to calculate the spin-exchange interactions of monolayer $X\mathrm{PS_3}$. The calculation results are shown in Fig. S2 in [43]. Note that, due to the strong SOC of $\mathrm{FePS_3}$, the $\mathrm{FePS_3}$ results are incorrect, i.e., the magnetic force theorem fails to calculate the $\mathrm{FePS_3}$ system [28]. It originates from the magnetic force theorem method treating the SOC effect as a perturbation. In this method, the nonrelativistic calculation always yields spin densities without orbital degrees of freedom. The effects of SOC are significant in $\mathrm{FePS_3}$, as they lead to large orbital moments, which are forbidden in nonrelativistic treatments. Thus, the basic assumption of the magnetic force theorem is no longer satisfied. In other words, the MAE of $\mathrm{FePS_3}$ should not be treated with the magnetic force theorem. However, the TB2J results of $\mathrm{NiPS_3}$ are in better agreement with the results of our MLMCH and four-state method. Most exchange interactions fall to small (but nonzero) values if the distance is larger than 9 Å.

We further discuss the underlying mechanism for the obtained large exchange interactions in $X\mathrm{PS_3}$ monolayers. The FM spin exchange between the nearest-neighbor pair competes with AFM third-neighbor exchange interactions. Our structure analysis shows that the bond angle of X-S-X is close to 90°, suggesting that the superexchange leads to the sizable first-NN FM exchange interaction. On the other hand, the indirect super-superexchange interaction result in the unusually large third-NN AFM exchange interaction. As for the biquadratic interaction K, the interesting phenomenon is that both $\mathrm{FePS_3}$ and $\mathrm{NiPS_3}$ have a large K.

Note that the SOC effects are different in the two materials. In $\mathrm{FePS_3}$, only one electron is filled in the doubly degenerate e_g' minority state, which results in a strong SOC effect, whereas the SOC is much weaker in $\mathrm{NiPS_3}$ owing to the fully filled doubly degenerate states. We additionally show in Fig. S3 in [43] the relative energies of various magnetic structures of $\mathrm{FePS_3}$ calculated without SOC. It is found that although the magnetic ground state is still an AFM-ZZ structure, the obtained exchange interactions are completely different from that obtained with SOC (Table SI in [43]). More importantly, the AFM-ZZ ground state cannot be obtained when such exchange interaction parameters are used in the Monte Carlo simulation [see Fig. S4(a) in [43]]. This result shows that the SOC effect cannot be ignored when investigating the magnetic properties of $\mathrm{FePS_3}$. It is also noticed that $\mathrm{FePS_3}$ has a robust out-of-plane magnetization, but $\mathrm{NiPS_3}$

TABLE I. The monolayer $X\mathrm{PS_3}$ lattice constants a (Å) are optimized. The bilinear exchange interactions (in meV) and NN biquadratic interaction (in meV) were calculated with the MLMCH (four-state method) for the monolayer $X\mathrm{PS_3}$. The SOC effect is included in $\mathrm{FePS_3}$. NA: Interaction does not exist in machine learning.

Material	a	J_1	J_2	J_3	K	A_z
$\mathrm{FePS_3}$	5.82	−2.20 (−2.10)	NA(0.10)	2.07 (2.18)	−2.69 (NA)	5.76 (4.88)
$\mathrm{NiPS_3}$	5.86	−3.60 (−3.38)	−0.60 (−0.64)	15.65 (15.79)	−1.56 (−1.66)	NA(−1.25)

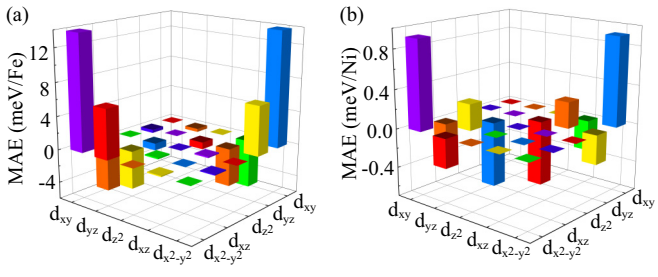

FIG. 2. Atomic orbital-resolved magnetocrystalline anisotropy energy difference of (a) the Fe atom in monolayer $FePS_3$ and (b) the Ni atom in monolayer $NiPS_3$.

exhibits an easy-plane magnetization. Considering the magnetic moment switching from the out-of-plane [001] axis to the in-plane [100] axis, the energy difference can be defined as the MAE, i.e., $E_{100} - E_{001}$. Generally, the MAE is induced by the crystal field splitting and SOC effect. In order to reveal the physical mechanism of the MAE difference between $FePS_3$ and $NiPS_3$, we perform analysis based on the second-order perturbation theory [45–47], where the MAE can be approximately described by

$$\begin{aligned}\Delta E^{sl} &= E_x^{sl} - E_z^{sl} \\ &= \xi^2 \sum_o \sum_u \frac{|\langle o|\mathbf{S_x}\cdot\mathbf{L_x}|u\rangle|^2 - |\langle o|\mathbf{S_z}\cdot\mathbf{L_z}|u\rangle|^2}{\varepsilon_o - \varepsilon_u},\end{aligned} \quad (2)$$

where E_x and E_z are the SOC energies for the x-axis and z-axis magnetization directions, respectively, and $|o\rangle$ and $|u\rangle$ denote the occupied and unoccupied states, respectively. According to Eq. (2), the MAE is determined by matrix elements of the spin-orbital interaction between occupied and unoccupied states.

Figure 2 and Fig. S5 in [43] show the calculated orbital-resolved MAE, where positive and negative values of MAE denote the out-of-plane and in-plane magnetizations, respectively. Clearly, the MAE mainly originates from Fe (in $FePS_3$) and Ni (in $NiPS_3$) atoms, while those from P and S atoms have minor contributions. In $FePS_3$, the d_{xy} and $d_{x^2-y^2}$, d_{yz}, and $d_{x^2-y^2}$ orbitals of Fe mainly contribute to the positive MAE values, whereas the d_{xy}, d_{xz}, d_{xz}, and d_{yz} orbitals contribute to the negative MAE values. This result strongly indicates that the $FePS_3$ monolayer possesses an out-of-plane magnetization. In $NiPS_3$, on the other hand, the d_{xy}, $d_{x^2-y^2}$, d_{xz}, and d_{yz} orbitals of Ni contribute to positive MAE values, while the remaining d orbitals give rise to negative MAE values. As a result of competition, the $NiPS_3$ exhibits an in-plane MAE.

The MAE can be further understand from the SOC formula. Generally, the $\hat{H}_{SO} = \lambda \hat{S}\cdot\hat{L}$ term can be written as [19,48,49]

$$\begin{aligned}\hat{H}_{SO} =& \lambda\hat{S}_{z'}\left(\hat{L}_z\cos\theta + \frac{1}{2}\hat{L}_+e^{-i\varphi}\sin\theta + \frac{1}{2}\hat{L}_-e^{i\varphi}\sin\theta\right) \\ &+ \frac{\lambda}{2}\hat{S}_{+'}\left(-\hat{L}_z\sin\theta - \hat{L}_+e^{-i\varphi}\sin^2\frac{\theta}{2} + \hat{L}_-e^{i\varphi}\cos^2\frac{\theta}{2}\right) \\ &+ \frac{\lambda}{2}\hat{S}_{-'}\left(-\hat{L}_z\sin\theta + \hat{L}_+e^{-i\varphi}\cos^2\frac{\theta}{2} - \hat{L}_-e^{i\varphi}\sin^2\frac{\theta}{2}\right).\end{aligned} \quad (3)$$

For a qualitative discussion of spin orientation, the SOC Hamiltonian $\hat{H}_{SO}$ can be rewritten as

$$\hat{H}_{SO} = \hat{H}^0_{SO} + \hat{H}^1_{SO}, \quad (4)$$

where $\hat{H}^0_{SO}$ is the spin-conserving term

$$\hat{H}^0_{SO} = \lambda\hat{S}_{z'}\left(\hat{L}_z\cos\theta + \tfrac{1}{2}\hat{L}_+e^{-i\varphi}\sin\theta + \tfrac{1}{2}\hat{L}_-e^{i\varphi}\sin\theta\right) \quad (5)$$

and $\hat{H}^1_{SO}$ is the spin-nonconserving term [19]. Since the lowest-energy gap between the occupied and unoccupied levels of XPS_3 occurs at a spin-down state, only the spin-conserving term is considered. For $FePS_3$, the Fe^{2+} (d^6) ion has the d-state splitting pattern $(e_{g'}\uparrow)^2 < (a_{1g}\uparrow)^1 < (e_g\uparrow)^2 < (e_{g'}\downarrow)^1 < (a_{1g}\downarrow)^0 < (e_g\downarrow)^0$. The lowest-energy gap between the occupied and unoccupied levels occurs in $(e_{g'}\downarrow)$. Since their m (magnetic quantum number) values are the same $\Delta m = 0$ they can interact when the spin direction is parallel to the orbital z axis. In other words, the preferred spin direction is parallel to the orbital z axis. We further consider the Ni^{2+} (d^8) ion of $NiPS_3$ with the d-electron configuration $(e_{g'}\uparrow)^2 < (a_{1g}\uparrow)^1 < (e_g\uparrow)^2 < (e_{g'}\downarrow)^2 < (a_{1g}\downarrow)^1 < (e_g\downarrow)^0$. Therefore, the lowest-energy gap occurs for the energy-level difference of $a_{1g}\downarrow$ and $e_g\downarrow$, because these two orbitals cannot interact due to the nonzero $\Delta m = 2$. The next-lowest-energy gap occurs for the $e_{g'}\downarrow$ and $e_g\downarrow$ levels, which can interact because their m values differ by ±1, namely, the preferred spin orientation is perpendicular to the z axis. Con-

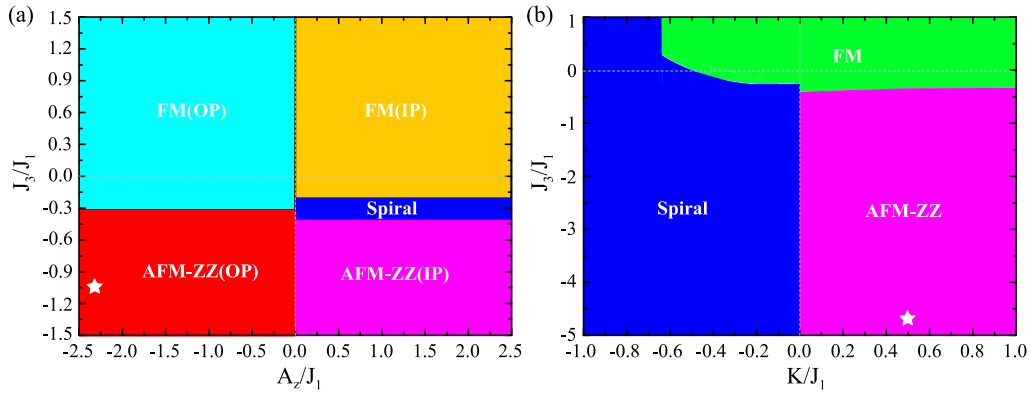

FIG. 3. Phase diagrams of (a) the J_1-J_3-A_z model for $FePS_3$ and (b) the J_1-K-J_3 model for $NiPS_3$. All simulations are based on $J_1 < 0$. The white pentagram represents the magnetic ground state.

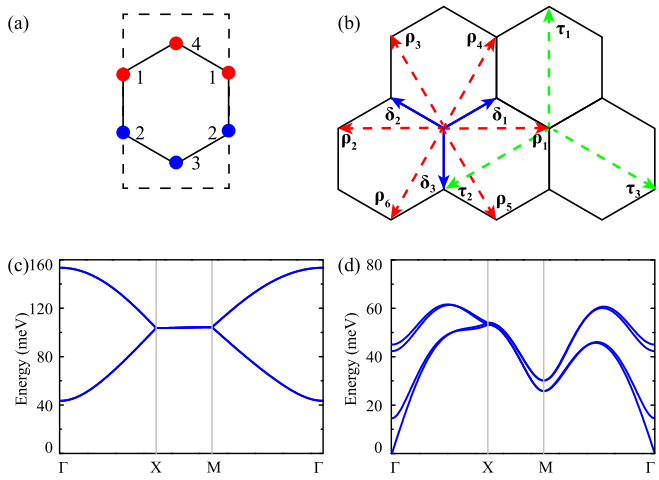

FIG. 4. (a) Sublattices inside the magnetic unit cell. The spin-up and spin-down X (X = Fe, Ni) atoms are depicted by the red and blue circles, respectively. (b) The δ, ρ, and τ are vectors joining the nearest-, second-nearest-, and third-nearest-neighbor X atoms. The spin-wave spectrum of (c) $FePS_3$ and (d) $NiPS_3$ is calculated using the LSWT method. The adopted magnetic interaction parameters are listed in Table I.

sequently, both theories above give rise to the same results, which perfectly reveal the physical origins of MAE in XPS_3.

B. Microscopic mechanisms of the AFM-ZZ state in XPS_3 (X = Fe, Ni) monolayers

In the above study, we have obtained the spin Hamiltonian by the calculations of the MLMCH. To determine the magnetic ground state of XPS_3 monolayers, we carried out PTMC simulations with spin Hamiltonian. More interestingly, although their spin Hamiltonians differ, the AFM-ZZ magnetic ground states are both obtained by the PTMC simulations (see Figs. S4 and S6 in [43]). In order to have a comprehensive understanding of the microscopic mechanism of the magnetic ground state of XPS_3 monolayers, we additionally calculate the phase diagram using the obtained spin Hamiltonian model (Fig. 3) and the PTMC simulations [38,39].

In $FePS_3$, the J_1-J_3-A_z terms are considered in the simulations. The J_1 and J_3 terms dominate magnetically ordered states and the A_z term determines the direction of magnetization. As shown in Fig. 3(a), when $A_z/J_1 < 0$, $FePS_3$ presents an out-of-plane FM state with $J_3/J_1 > -0.33$, whereas the out-of-plane AFM-ZZ state appears when increasing the AFM interaction ($J_3/J_1 < -0.33$). On the other hand, in the region $A_z/J_1 > 0$, there are two transition points, i.e., the in-plane FM to spiral state and the spiral to in-plane AFM-ZZ state. Such phase transitions occur around $J_3/J_1 \simeq -0.20$ and -0.40, respectively. We additionally explore the effect of biquadratic interaction K on the magnetic ground state of $FePS_3$ by changing K from -2.69 meV to 2.69 meV and keeping $J_1 = -2.20$ and 2.07 meV and $A_z = 5.76$ meV. The calculated results show that the magnetic ground state remains an AFM-ZZ structure when $K < 0$ meV, while it will become a spiral state if $K > 0$ meV. Hence, negative biquadratic interaction mainly has the effect of keeping the magnetic ground state collinear in $FePS_3$.

As for $NiPS_3$, the J_1-K-J_3 model is adopted, due to the significant biquadratic interaction. As shown in Fig. 3(b), in the case of $K/J_1 < 0$, the FM state exists only in a small region and the remaining regions are spiral states. When $K/J_1 > 0$, the FM order exists with $J_3/J_1 > -0.33$. There is also a transition from a FM to an AFM-ZZ state with $J_3/J_1 < -0.33$. The above results show that the third-NN AFM Heisenberg interaction J_3 and first-NN FM biquadratic interaction K are crucial factors for the formation of AFM-ZZ order.

C. Spin-wave spectrum

The obtained spin Hamiltonian allows us to make an accurate prediction about the spin-wave spectrum of XPS_3 monolayers. The spin-wave spectrum can be calculated by using the LSWT method [41,50–52], where the linearized Holstein-Primakoff transformation is adopted,

$$\hat{S}_i^+ = \sqrt{\frac{S}{2}}(\hat{b}_i^\dagger + \hat{b}_i),$$
$$\hat{S}_i^- = i\sqrt{\frac{S}{2}}(\hat{b}_i^\dagger - \hat{b}_i),$$
$$\hat{S}_i^z = S - \hat{b}_i^\dagger \hat{b}_i. \tag{6}$$

Here $\hat{b}_i^\dagger$ and $\hat{b}_i$ are the bosonic creation and annihilation operators on the site i, respectively. The representation of the spin Hamiltonian (6) in terms of this bosonic operators leads to a complicated nonlinear Hamiltonian. In the spin-wave linear approximation, the higher-order terms are neglected.

In the zigzag ordered materials, it has a doubled unit cell consisting of four lattice sites and a spin configuration, as shown in Fig. 4(a). For $FePS_3$, the effective Hamiltonian in momentum space is written as (for derivation of the Hamiltonian, see the Supplemental Material [43])

$$\hat{\mathrm{H}}(\mathbf{k}) = \begin{pmatrix} f_1(\mathbf{k}) & f_2(\mathbf{k}) & 0 & 0 & 0 & 0 & f_3(\mathbf{k}) & f_4(\mathbf{k}) \\ f_2^*(\mathbf{k}) & f_1(\mathbf{k}) & 0 & 0 & 0 & 0 & f_4^*(\mathbf{k}) & f_3(\mathbf{k}) \\ 0 & 0 & f_1(\mathbf{k}) & f_2(\mathbf{k}) & f_3^*(\mathbf{k}) & f_4(\mathbf{k}) & 0 & 0 \\ 0 & 0 & f_2^*(\mathbf{k}) & f_1(\mathbf{k}) & f_4^*(\mathbf{k}) & f_3^*(\mathbf{k}) & 0 & 0 \\ 0 & 0 & f_3(\mathbf{k}) & f_4(\mathbf{k}) & f_1^*(\mathbf{k}) & f_2(\mathbf{k}) & 0 & 0 \\ 0 & 0 & f_4^*(\mathbf{k}) & f_3(\mathbf{k}) & f_2^*(\mathbf{k}) & f_1^*(\mathbf{k}) & 0 & 0 \\ f_3^*(\mathbf{k}) & f_4(\mathbf{k}) & 0 & 0 & 0 & 0 & f_1^*(\mathbf{k}) & f_2(\mathbf{k}) \\ f_4^*(\mathbf{k}) & f_3^*(\mathbf{k}) & 0 & 0 & 0 & 0 & f_2^*(\mathbf{k}) & f_1^*(\mathbf{k}) \end{pmatrix}, \tag{7}$$

where $f_1(\mathbf{k}) = -J_1S - 6KS^3 + (2+\xi_{1\mathbf{k}})J_2S + 3J_3S + A_zS$, $f_2(\mathbf{k}) = (J_1S + 2KS^3)\gamma_{1\mathbf{k}}$, $f_3(\mathbf{k}) = J_2S\xi_{2\mathbf{k}}$, and $f_4(\mathbf{k}) = (J_1S - 2KS^3)\gamma_{2\mathbf{k}} + J_3S\gamma_{\mathbf{k}}$. The explicit forms of the structure factors $\gamma_{\mathbf{k}}, \gamma_{1\mathbf{k}}, \gamma_{2\mathbf{k}}, \xi_{1\mathbf{k}}, \xi_{1\mathbf{k}}$ are presented in the Supplemental Material [43]. Following, we calculate the magnon band structure of $FePS_3$ using the parameters obtained by the MLMCH, as shown in Fig. 4(c). It shows that the out-of-plane single-ion anisotropy will open a spin-wave gap 43.50 meV in $FePS_3$. Moreover, we find that the spectrum is fourfold degenerate along the X-M line, which splits into two doubly degenerate bands on the Γ-X and M-Γ lines due to the out-of-plane anisotropy. On the X-M line, $(T\bar{M}_y)^2 = -1$, indicating a Kramers degeneracy. On the other hand, $T\bar{M}_y$ commutes with S_x, indicating the Kramers pair is within the same eigenspace of S_x. In addition, the spin-wave spectrum has two branches at the Γ point. Based on the magnetic point group, the lower-energy magnon is the Raman-active A_g mode, while the higher-energy magnon belongs to representation B_u [53]. This result is completely consistent with previous experimental reports [53].

Although $NiPS_3$ has a structure similar to $FePS_3$, the spin direction of the magnetic ground state lies in the ab plane, different from that of $FePS_3$. Hence, $NiPS_3$ has a different Hamiltonian (for derivation of the Hamiltonian, see the Supplemental Material [43]) that can be written as

$$\hat{\mathrm{H}}(\mathbf{k}) = \begin{pmatrix} g_1(\mathbf{k}) & g_2(\mathbf{k}) & 0 & 0 & g_5(\mathbf{k}) & 0 & g_3(\mathbf{k}) & g_4(\mathbf{k}) \\ g_2^*(\mathbf{k}) & g_1(\mathbf{k}) & 0 & 0 & 0 & g_5(\mathbf{k}) & g_4^*(\mathbf{k}) & g_3(\mathbf{k}) \\ 0 & 0 & g_1(\mathbf{k}) & g_2(\mathbf{k}) & g_3^*(\mathbf{k}) & g_4(\mathbf{k}) & g_5(\mathbf{k}) & 0 \\ 0 & 0 & g_2^*(\mathbf{k}) & g_1(\mathbf{k}) & g_4^*(\mathbf{k}) & g_3^*(\mathbf{k}) & 0 & g_5(\mathbf{k}) \\ g_5^*(\mathbf{k}) & 0 & g_3(\mathbf{k}) & g_4(\mathbf{k}) & g_1^*(\mathbf{k}) & g_2(\mathbf{k}) & 0 & 0 \\ 0 & g_5^*(\mathbf{k}) & g_4^*(\mathbf{k}) & g_3(\mathbf{k}) & g_2^*(\mathbf{k}) & g_1^*(\mathbf{k}) & 0 & 0 \\ g_3^*(\mathbf{k}) & g_4(\mathbf{k}) & g_5^*(\mathbf{k}) & 0 & 0 & 0 & g_1^*(\mathbf{k}) & g_2(\mathbf{k}) \\ g_4^*(\mathbf{k}) & g_3^*(\mathbf{k}) & 0 & g_5^*(\mathbf{k}) & 0 & 0 & g_2^*(\mathbf{k}) & g_1^*(\mathbf{k}) \end{pmatrix}, \tag{8}$$

where $g_1(\mathbf{k}) = -J_1 - 6KS^3 + (2+\xi_{1\mathbf{k}})J_2S + 3J_3S - \frac{1}{2}A_zS$, $g_2(\mathbf{k}) = (J_1S + 2KS^3)\gamma_{1\mathbf{k}}$, $g_3(\mathbf{k}) = -J_2S\xi_{2\mathbf{k}}$, $g_4(k) = (-J_1S + 2KS^3)\gamma_{2\mathbf{k}} - J_3S\gamma_{\mathbf{k}}$, and $g_5(\mathbf{k}) = -\frac{1}{2}A_zS$. The explicit forms of the structure factors $\gamma_{\mathbf{k}}, \gamma_{1\mathbf{k}}, \gamma_{2\mathbf{k}}, \xi_{1\mathbf{k}}, \xi_{1\mathbf{k}}$ are listed in the Supplemental Material [43]. As shown in Fig. 4(d), we employ the Heisenberg exchange parameter by the MLMCH and single-ion anisotropy parameter by the four-state method to calculate the magnon band structure of $NiPS_3$. It is seen that when the direction of easy magnetization is turned in-plane, the spin-wave gap will disappear in $NiPS_3$. Moreover, the double degeneracy of spin-wave spectrum is broken and simultaneously an hourglass band appears in the $\Gamma - X$ direction of the high symmetry line. This originates from the fact that S_x is no longer a good quantum number. The calculated spin-wave spectrum provides a theoretical guidance for the experimental investigation of the magnetic dynamics of 2D XPS_3.

IV. CONCLUSION

In summary, to understand the microscopic mechanisms of the AFM-ZZ ground state in the XPS_3 (X = Fe, Ni) monolayer system, we construct the spin Hamiltonian by combining first-principles calculations and the newly developed machine learning method. In this spin Hamiltonian, we have successfully unveiled the magnetic interactions of the XPS_3 system. We find found that the AFM-ZZ ground state within the $FePS_3$ monolayer is stabilized by competing ferromagnetic nearest-neighbor and antiferromagnetic third-nearest-neighbor exchange interactions and combining single-ion anisotropy. However, the often ignored nearest-neighbor biquadratic exchange is a crucial interaction for the stabilization of the AFM-ZZ order within $NiPS_3$. By adopting our model, one can also accurately calculate the spin wave, which paves a way for future experimental study of magnetic excitations in XPS_3 systems. We believe that the exact spin Hamiltonian discovered in this study could be widely used in understanding magnetic interactions of two-dimensional materials.

ACKNOWLEDGMENTS

We acknowledge financial support from the Ministry of Science and Technology of the People's Republic of China (Grant No. 2022YFA1402901) and the National Natural Science Foundation of China (Grants No. 11825403, No. 12074301, and No. 12004295). P.L. also acknowledge support from the China's Postdoctoral Science Foundation funded project (Grant No. 2022M722547), the Fundamental Research Funds for the Central Universities (Grant No. xxj03202205), and the Open Project of State Key Laboratory of Surface Physics (Grant No. KF2024_02).

[1] K. S. Novoselov, A. K. Geim, S. V. Morozov, D. Jiang, Y. Zhang, S. V. Dubonos, I. V. Grigorieva, and A. A. Firsov, Electric field effect in atomically thin carbon films, Science **306**, 666 (2004).

[2] K. S. Novoselov, A. K. Geim, S. V. Morozov, D. Jiang, M. I. Katsnelson, I. V. Grigorieva, S. V. Dubonos, and A. A. Firsov, Two-dimensional gas of massless Dirac fermions in graphene, Nature (London) **438**, 197 (2005).

[3] Y. Zhang, Y. W. Tan, H. L. Stormer, and P. Kim, Experimental observation of the quantum Hall effect and Berry's phase in graphene, Nature (London) **438**, 201 (2005).

[4] A. H. Castro Neto, F. Guinea, N. M. R. Peres, K. S. Novoselov, and A. K. Geim, The electronic properties of graphene, Rev. Mod. Phys. **81**, 109 (2009).

[5] Y. Cao, V. Fatemi, S. Fang, K. Watanabe, T. Taniguchi, E. Kaxiras, and P. Jarillo-Herrero, Unconventional superconductivity in magic-angle graphene superlattices, Nature (London) **556**, 43 (2018).

[6] Y. Xu, K. Kang, K. Watanabe, T. Taniguchi, K. F. Mak, and J. Shan, A tunable bilayer Hubbard model in twisted WSe_2, Nat. Nanotechnol. **17**, 934 (2022).

[7] P. Li, X. Yang, Q. S. Jiang, Y. Z. Wu, and W. Xun, Built-in electric field and strain tunable valley-related multiple topological phase transitions in $VSiXN_4$(X = C, Si, Ge, Sn, Pb) monolayers, Phys. Rev. Mater. **7**, 064002 (2023).

[8] P. Li, C. Wu, C. Peng, M. Yang, and W. Xun, Multifield tunable valley splitting in two-dimensional MXene Cr_2COOH, Phys. Rev. B **108**, 195424 (2023).

[9] W. Xun, C. Wu, H. Sun, W. Zhang, Y. Z. Wu, and P. Li, Coexisting magnetism, ferroelectric, and ferrovalley multiferroic in stacking-dependent two-dimensional materials, Nano Lett. **24**, 3541 (2024).

[10] C. Gong, L. Lin, Z. Li, H. Ji, A. Stern, Y. Xia, T. Cao, W. Bao, C. Wang, Y. Wang, Z. Q. Qiu, R. J. Cava, S. G. Louie, J. Xia, and X. Zhang, Discovery of intrinsic ferromagnetism in two-dimensional van der Waals crystals, Layer-dependent ferromagnetism in a van der Waals crystal down to the monolayer limit, Nature (London) **546**, 265 (2017).

[11] B. Huang, G. Clark, E. N. Moratalla, D. R. Klein, R. Cheng, K. L. Seyler, D. Zhong, E. Schmidgall, M. A. McGuire, D. H. Cobden, W. Yao, D. Xiao, P. Jarillo-Herrero, and X. Xu, Layer-dependent ferromagnetism in a van der Waals crystal down to the monolayer limit, Nature (London) **546**, 270 (2017).

[12] J. M. Lu, O. Zheliuk, I. Leermakers, N. F. Q. Yuan, U. Zeitler, K. T. Law, and J. T. Ye, Evidence for two-dimensional Ising superconductivity in gated MoS_2, Science **350**, 1353 (2015).

[13] M. M. Ugeda, A. J. Bradley, Y. Zhang, S. Onishi, Y. Chen, W. Ruan, C. O. Aristizabal, H. Ryu, M. T. Edmonds, H. Z. Tsai, A. Riss, S. K. Mo, D. Lee, A. Zettl, Z. Hussain, Z. X. Shen, and M. F. Crommie, Characterization of collective ground states in single-layer $NbSe_2$, Nat. Phys. **12**, 92 (2016).

[14] X. Xi, L. Zhao, Z. Wang, H. Berger, L. Forro, J. Shan, and K. F. Mak, Strongly enhanced charge-density-wave order in monolayer $NbSe_2$, Nat. Nanotechnol. **10**, 765 (2015).

[15] Y. Ren, Z. Qiao, and Q. Niu, Topological phases in two-dimensional materials: A review, Rep. Prog. Phys. **79**, 066501 (2016).

[16] K. Chang, J. Liu, H. Lin, N. Wang, K. Zhao, A. Zhang, F. Jin, Y. Zhong, X. Hu, W. Duan, Q. Zhang, L. Fu, Q. K. Xue, X. Chen, and S. H. Ji, Discovery of robust in-plane ferroelectricity in atomic-thick SnTe, Science **353**, 274 (2016).

[17] K. Liu, J. Lu, S. Picozzi, L. Bellaiche, and H. J. Xiang, Intrinsic origin of enhancement of ferroelectricity in SnTe ultrathin films, Phys. Rev. Lett. **121**, 027601 (2018).

[18] Y. K. Zhang, Q. Yang, L. L. Tao, and E. Y. Tsymbal, Effects of strain and film thickness on the stability of the rhombohedral phase of HfO_2, Phys. Rev. Appl. **14**, 014068 (2020).

[19] H. J. Xiang, C. Lee, H. J. Koo, X. Gong, and M. H. Whangbo, Magnetic properties and energy-mapping analysis, Dalton Trans. **42**, 823 (2013).

[20] G. Ouvrard, R. Brec, and J. Rouxel, Structural determination of some MPS_3 layered phases (M = Mn, Fe, Co, Ni and Cd), Mater. Res. Bull. **20**, 1181 (1985).

[21] J. U. Lee, S. Lee, J. H. Ryoo, S. Kang, T. Y. Kim, P. Kim, C. H. Park, J. G. Park, and H. Cheong, Ising-type magnetic ordering in atomically thin $FePS_3$, Nano Lett. **16**, 7433 (2016).

[22] D. Lançon, H. C. Walker, E. Ressouche, B. Ouladdiaf, K. C. Rule, G. J. McIntyre, T. J. Hicks, H. M. Ronnow, and A. R. Wildes, Magnetic structure and magnon dynamics of the quasi-two-dimensional antiferromagnet $FePS_3$, Phys. Rev. B **94**, 214407 (2016).

[23] M. J. Coak, D. M. Jarvis, H. Hamidov, A. R. Wildes, J. A. M. Paddison, C. Liu, C. R. S. Haines, N. T. Dang, S. E. Kichanov, B. N. Savenko, S. Lee, M. Kratochvilova, S. Klotz, T. C. Hansen, D. P. Kozlenko, J. G. Park, and S. S. Saxena, Emergent magnetic phases in pressure-tuned van der Waals antiferromagnet $FePS_3$, Phys. Rev. X **11**, 011024 (2021).

[24] A. Pawbake, T. Pelini, A. Delhomme, D. Romanin, D. Vaclavkova, G. Martinez, M. Calandra, M. A. Measson, M. Veis, M. Potemski, M. Orlita, and C. Faugeras, High-pressure tuning of magnon-polarons in the layered antiferromagnet $FePS_3$, ACS Nano **16**, 12656 (2022).

[25] K. Kim, S. Y. Lim, J. U. Lee, S. Lee, T. Y. Kim, K. Park, G. S. Jeon, C. H. Park, J. G. Park, and H. Cheong, Suppression of magnetic ordering in XXZ-type antiferromagnetic monolayer $NiPS_3$, Nat. Commun. **10**, 345 (2019).

[26] C. Lane and J. X. Zhu, Thickness dependence of electronic structure and optical properties of a correlated van der Waals antiferromagnetic $NiPS_3$ thin film, Phys. Rev. B **102**, 075124 (2020).

[27] A. R. Wildes, J. R. Stewart, M. D. Le, R. A. Ewings, K. C. Rule, G. Deng, and K. Anand, Magnetic dynamics of $NiPS_3$, Phys. Rev. B **106**, 174422 (2022).

[28] T. Y. Kim and C. H. Park, Magnetic anisotropy and magnetic ordering of transition-metal phosphorus trisulfides, Nano Lett. **21**, 10114 (2021).

[29] M. Amirabbasi and P. Kratzer, Orbital and magnetic ordering in single-layer $FePS_3$: A DFT+U study, Phys. Rev. B **107**, 024401 (2023).

[30] X. Li, F. Lou, X. G. Gong, and H. J. Xiang, Constructing realistic effective spin Hamiltonians with machine learning approaches, New J. Phys. **22**, 053036 (2020).

[31] P. E. Blöchl, Projector augmented-wave method, Phys. Rev. B **50**, 17953 (1994).

[32] G. Kresse and J. Furthmuller, Efficient iterative schemes for *ab initio* total-energy calculations using a plane-wave basis set, Phys. Rev. B **54**, 11169 (1996).

[33] V. I. Anisimov, F. Aryasetiawan, and A. I. Lichtenstein, First-principles calculations of the electronic structure and spectra of strongly correlated systems: the LDA + U method, J. Phys.: Condens. Matter **9**, 767 (1997).

[34] J. P. Perdew, K. Burke, and M. Ernzerhof, Generalized gradient approximation made simple, Phys. Rev. Lett. **77**, 3865 (1996).

[35] Y. Gu, Q. Zhang, C. Le, Y. Li, T. Xiang, and J. Hu, Ni-based transition metal trichalcogenide monolayer: A strongly correlated quadruple-layer graphene, Phys. Rev. B **100**, 165405 (2019).

[36] J. Y. Ni, X. Y. Li, D. Amoroso, X. He, J. S. Feng, E. J. Kan, S. Picozzi, and H. J. Xiang, Giant biquadratic exchange in 2D magnets and its role in stabilizing ferromagnetism of $NiCl_2$ monolayers, Phys. Rev. Lett. **127**, 247204 (2021).

[37] H. J. Xiang, E. J. Kan, S. H. Wei, M. H. Whangbo, and X. G. Gong, Predicting the spin-lattice order of frustrated systems from first principles, Phys. Rev. B **84**, 224429 (2011).

[38] P. S. Wang and H. J. Xiang, Room-temperature ferrimagnet with frustrated antiferroelectricity: Promising candidate toward multiple-state memory, Phys. Rev. X **4**, 011035 (2014).

[39] K. Hukushima and K. Nemoto, Exchange Monte Carlo method and application to spin glass simulations, J. Phys. Soc. Jpn. **65**, 1604 (1996).

[40] F. Lou, X. Y. Li, J. Y. Ji, H. Y. Yu, J. S. Feng, X. G. Gong, and H. J. Xiang, PASP: Property analysis and simulation package for materials, J. Chem. Phys. **154**, 114103 (2021).

[41] S. Toth and B. Lake, Linear spin wave theory for single-Q incommensurate magnetic structures, J. Phys.: Condens. Matter **27**, 166002 (2015).

[42] LDA $+U$+SOC ($FePS_3$) or GGA $+U$ ($NiPS_3$) calculations using the structure optimized with the FM order, and full LDA $+U$+SOC ($FePS_3$) or GGA $+U$ ($NiPS_3$) calculations in which the structures are optimized with the corresponding magnetic orders.

[43] See Supplemental Material at http://link.aps.org/supplemental/10.1103/PhysRevB.109.214418 for the relative energies of $FePS_3$ with different procedures, the magnetic exchange interactions by the TB2J method, the magnetic ground state of XPS_3 by the PTMC simulation, the atomic orbital-resolved magnetocrystalline anisotropy energy difference of XPS_3, the exchange interactions without the SOC effect for $FePS_3$, and the linear spin wave theory of XPS_3.

[44] X. Hu, N. Helbig, M. J. Verstraete, and E. Bousquet, TB2J: A Python package for computing magnetic interaction parameters, Comput. Phys. Commun. **264**, 107938 (2021).

[45] D. S. Wang, R. Q. Wu, and A. J. Freeman, First-principles theory of surface magnetocrystalline anisotropy and the diatomic-pair model, Phys. Rev. B **47**, 14932 (1993).

[46] J. Hu and R. Q. Wu, Control of the magnetism and magnetic anisotropy of a single-molecule magnet with an electric field, Phys. Rev. Lett. **110**, 097202 (2013).

[47] J. Hu and R. Q. Wu, Giant magnetic anisotropy of transition-metal dimers on defected graphene, Nano Lett. **14**, 1853 (2014).

[48] X. Wang, R. Wu, D. S. Wang, and A. J. Freeman, Torque method for the theoretical determination of magnetocrystalline anisotropy, Phys. Rev. B **54**, 61 (1996).

[49] D. Dai, H. J. Xiang, and M. H. Whangbo, Effects of spin-orbit coupling on magnetic properties of discrete and extended magnetic systems, J. Comput. Chem. **29**, 2187 (2008).

[50] F. Kargar, E. A. Coleman, S. Ghosh, J. Lee, M. J. Gomez, Y. Liu, A. S. Magana, Z. Barani, A. Mohammadzadeh, B. Debnath, R. B. Wilson, R. K. Lake, and A. A. Balandin, Phonon and thermal properties of quasi-two-dimensional $FePS_3$ and $MnPS_3$ antiferromagnetic semiconductors, ACS Nano **14**, 2424 (2020).

[51] Q. Zhang, K. Hwangbo, C. Wang, Q. Jiang, J. H. Chu, H. Wen, X. Xiao, and X. Xu, Observation of giant optical linear dichroism in a zigzag antiferromagnet $FePS_3$, Nano Lett. **21**, 6938 (2021).

[52] Y. S. Hou, H. J. Xiang, and X. G. Gong, Unveiling magnetic interactions of ruthenium trichloride via constraining direction of orbital moments: Potential routes to realize a quantum spin liquid, Phys. Rev. B **96**, 054410 (2017).

[53] S. Liu, A. G. del Aguila, D. Bhowmick, C. K. Gan, T. T. Ha Do, M. A. Prosnikov, D. Sedmidubsky, Z. Sofer, P. C. M. Christianen, P. Sengupta, and Q. Xiong, Direct observation of magnon-phonon strong coupling in two-dimensional antiferromagnet at high magnetic fields, Phys. Rev. Lett. **127**, 097401 (2021).